PCCP

Cite this: *Phys. Chem. Chem. Phys.*, 2011, **13**, 18910–18920

www.rsc.org/pccp

PAPER

Deeply bound cold caesium molecules formed after 0_g^- resonant coupling

H. Lignier, A. Fioretti,* R. Horchani, C. Drag, N. Bouloufa, M. Allegrini,† O. Dulieu, L. Pruvost, P. Pillet and D. Comparat

Received 9th May 2011, Accepted 4th July 2011
DOI: 10.1039/c1cp21488h

Translationally cold caesium molecules are created by photoassociation below the $6s + 6p_{1/2}$ excited state and selectively detected by resonance enhanced two photon ionization (RE2PI). A series of excited vibrational levels belonging to the 0_g^- symmetry is identified. The regular progression of the vibrational spacings and of the rotational constants of the 0_g^- ($6s + 6p_{1/2}$) levels is strongly altered in two energy domains. These deviations are interpreted in terms of resonant coupling with deeply bound energy levels of two upper 0_g^- states dissociating into the $6s + 6p_{3/2}$ and $6s + 5d_{3/2}$ asymptotes. A theoretical model is proposed to explain the coupling and a quantum defect analysis of the perturbed level position is performed. Moreover, the resonant coupling changes dramatically the spontaneous decay products of the photoexcited molecules, strongly enhancing the decay into deeply bound levels of the $a^3\Sigma_u^+$ triplet state and of the $X^1\Sigma_g^+$ ground state. These results may be relevant when conceiving population transferring schemes in cold molecule systems.

1 Introduction

Cold and ultracold molecules have received increasing attention in recent years due to significant advances and potential new applications they offer in several directions: ultra-high resolution molecular spectroscopy, tests of fundamental theories in physics, clocks based on molecular transitions, full control of the dynamics of cold chemical reactions, and design of quantum information devices.[1–4] Among the various approaches to form stable cold molecules, the photoassociation (PA) of laser-cooled atoms into an excited molecule followed by stabilization *via* spontaneous emission has proven very successful to obtain large and dense samples of ultracold homonuclear and heteronuclear alkali dimers.[3] Ultracold molecules in the lowest rovibrational level of their electronic ground state have been observed in this way,[5,6] through subsequent vibrational cooling using a femtosecond laser,[7,8] and by combining PA with the Stimulated Raman Adiabatic Passage (STIRAP) method.[9] Spectacular developments have also been achieved through the control of Feshbach resonances of ultracold colliding alkali atoms with external magnetic fields in combination with the STIRAP method to create ultracold molecules in their absolute ground state level.[10,11]

In order to have control of the final molecular quantum state, a precise knowledge of the relevant potential energy surfaces and of their interactions is necessary. Different high-resolution spectroscopic techniques, such as PA, Fourier transform, single photon and two-photon resonance spectroscopy, provide a wealth of information about molecular energy surfaces.[12] With this information, coherent as well as incoherent quantum state transfer processes can be engineered using suitable laser beams and different electromagnetic fields. The efficiency of a transition to a possible final state is limited by selection rules on angular momentum, parity and spin as well as by the overlap between the wavefunctions of the two levels, the square of which is called the Frank–Condon (FC) factor.[12] Several interactions can couple potential surfaces of different electronic states, thus giving the opportunity to override these limits. As a consequence, the related energy spectra of the involved molecular states are perturbed. Relatively large energy shifts and rotational constant variations are expected for levels of coupled states sharing the same energy range.[13] In the cold molecule domain, such 'resonant' coupling between vibrational levels induced by the interaction of two (or more) electronic states[14] has been observed for both caesium and rubidium dimers, giving rise to a significant and unexpected enhancement of cold molecule formation.[15–18] Prospective studies of resonant coupling in cold heteronuclear alkali dimers also recently appeared.[19,20] Note that coupling between electronic states but with no direct interaction between energy levels is invoked for the formation of ultracold RbCs[21] and KRb[10] ground states molecules.

The work presented here reports on high-resolution spectroscopic results concerning the 0_g^- attractive state of the caesium dimer correlated to the $6s + 6p_{1/2}$ excited asymptote. Although this energy region has been already investigated in photoassociation experiments[22] and in analysis,[23,24] here we have for the first time the possibility to study the complete reaction mechanism by performing high resolution PA spectroscopy and

Laboratoire Aimé Cotton, CNRS, Univ. Paris Sud, bât. 505, Campus d'Orsay, 91405, Orsay Cedex, France.
E-mail: andrea.fioretti@lac.u-psud.fr
† Permanent address: CNISM, Dipartimento di Fisica, Università di Pisa, Largo B. Pontecorvo, 56127 Pisa, Italy.

by analyzing spectroscopically the final states and vibrational levels of the molecules after the radiative stabilization. In this way we can isolate two subtle mechanisms, a three-state resonant coupling in the excitation and a two-photon decay that make this experiment a paradigm for cold molecule formation experiments. We are able to probe efficiently the molecular population of the vibrational levels of both the lowest triplet state $a^3\Sigma_u^+$ (hereafter simply referred as a) and the singlet ground state $X^1\Sigma_g^+$ (hereafter simply referred as X). We can thus detect 20 high-lying vibrational levels belonging to the 0_g^- ($6s + 6p_{1/2}$) state.

Both vibrational and rotational progressions appear to be perturbed by the presence of two vibrational levels belonging to a higher lying 0_g^- state. The positions of the perturbing levels are deduced through a Lu–Fano analysis.[25,26] The analysis[23,24] of data of ref. 22 already showed a perturbation in the progression of the binding energies of the 0_g^- ($6s + 6p_{1/2}$) vibrational levels. We were able to record energy positions with a high accuracy and thus measure the rotational constants for many observed lines.

The effect of the perturbing levels not only alters the spectroscopic signature (position and rotational constant) of the levels but also changes completely the radiative decay paths to the ground states. While unperturbed 0_g^- levels mainly decay into high lying levels of the a state, the perturbed ones preferentially either decay into much more deeply bound levels of the a state, or undergo a two-photon decay into deeply bound levels of the X singlet ground state (see Fig. 1). In particular we observe a large decay towards the first 60 vibrational levels of the X state. Similar two-photon decay mechanisms have been observed starting from different excited states[18,27] and also proposed in ref. 28. These observations, which can probably be generalized to other homonuclear and heteronuclear cold molecular species, will be useful for the engineering of quantum state transfer schemes. They contribute to pave the way towards the production of cold molecular samples with an extreme control over external as well as internal degrees of freedom.

The paper is organized as follows: in Section 2 we describe the experimental setup and the excitation and detection mechanisms. In Section 3 we report the results, *i.e.* the spectroscopic analysis and the selective detection of deeply bound ground state molecules. In Section 4 we present a spectroscopic analysis based on the vibrational quantum defect while in Section 5 we discuss a theoretical model explaining the whole process. Conclusions and prospects are reported in Section 6.

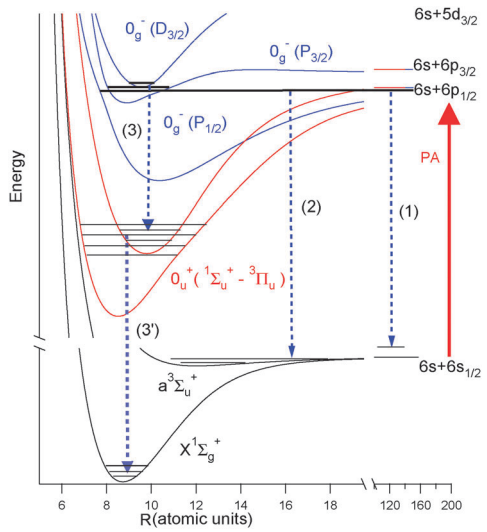

Fig. 1 (color online) The cold molecule formation scheme. Atom pairs are associated by the PA laser. Three different decay processes are possible, leading respectively to: two free atoms (1), triplet ground state molecules (2) and singlet molecules (3-3′). More details are given in the text.

2 Experiment

The experimental setup has been described in greater detail in ref. 7, 8, 29 and 30. Briefly, a sample of $N \approx 10^7$ laser-cooled caesium atoms is trapped in a standard MOT, at a density $n > 10^{10}$ cm^{-3} and at temperature $T \approx 100$ μK. The accurate values of these quantities are not measured because the MOT parameters are optimized directly on the signal to noise ratio of the photoassociation signal. An intense laser ($\sim$300 W cm^{-2}) induces PA transitions to excited state molecular levels in the 11125–11175 cm^{-1} range. These molecules either decay into two free atoms or into ground state dimers, leading in both cases to trap losses. Cold molecules are not trapped and slowly undergo a ballistic expansion under gravity. They are available in the interaction volume for about 10 ms for further study and detection. Cold ground state molecules are detected after pulsed two-photon photoionization, in the 15 700–16 100 cm^{-1} range, into Cs_2^+ molecular ions. They are accelerated to a pair of microchannel plates, being time-of-flight separated from atomic ions.

By tuning the frequency of the photoassociation laser a target molecular state is selected and, after spontaneous decay, ground state molecules can be formed. When molecules are produced in the deepest bound levels (roughly $v_X = 0$–30) of the singlet X state, a vibrational cooling phase can be added to pump most of these molecules into a single selected level, normally $v_X = 0$. This is accomplished either with a shaped femtosecond laser[7,8] or simply with a broadband diode laser.[29]

An extensive PA spectroscopy of the 4 attractive Hund's (c) case states (0_g^- 0_u^+ 1_u and 1_g) dissociating to the $6s + 6p_{3/2}$ asymptote has been done in the past,[31] as well as 2-color PA spectroscopy of the last bound levels of the lower triplet state.[32] Here, we do not intend to perform extensive spectroscopy of molecular states below the $6s + 6p_{1/2}$ asymptote, already reported in ref. 22. Rather, we utilise spectroscopy to put in evidence a subtle coupling mechanism between three 0_g^- potential surfaces leading to interesting quantum state transfer. The PA laser is set to excite at long range vibrational levels belonging to the $0_g^-(6s + 6p_{1/2})$ state, in the first 20 cm^{-1} below the atomic asymptote. This series had already been observed several years ago in Laboratoire Aimé Cotton[33] and more recently in the University of Connecticut at Storrs.[22]

PA to the $0_g^-(6s + 6p_{1/2})$ state and the cold molecule formation scheme is represented in Fig. 1. In this region these levels are coupled to some inner ones, presumably belonging to the upper $0_g^-(6s + 6p_{3/2})$ and $0_g^-(6s + 5d_{3/2})$ states (see Section 5). Excited molecules may decay at long range into

two free hot atoms (process 1) or, alternatevely into ground state dimers (processes 2 and 3–3′). In either case photo-associated atoms are lost from the MOT and a decrease in fluorescence can be observed, giving rise to trap loss spectrum.

The 0_g^- being a state of *gerade* symmetry, any one-photon spontanous decay ends up either (process 2) into the *a* ground state or into the $\Omega = 0_u^{+/-}$, 1_u and 2_u components of the $b^3\Pi_u$ state, located at intermediate energies (process 3). Selection rules on *g*/*u* parity and total spin conservation should make the latter state metastable. Nevertheless, a resonant coupling with the $0_u^+(A^1\Sigma_u^+)$ state can allow a further decay of the $0_u^+(b^3\Pi_u)$ component into the *X* ground state (process 3′).[28] This two-photon decay is indeed present since ground state *X* levels are observed. It seems favored at shorter internuclar distances but the relative efficiency of the two processes (2 and 3–3′) has to be discussed.

2.1 Selective ionization spectroscopy

Ground state cold molecules can be efficiently ionized into Cs_2^+ ions by the Resonance Enhanced 2-Photon Ionization (RE2PI) process proceeding through different intermediate molecular states. Several detection schemes have been used at different laser energies. In particular, all the schemes detecting caesium molecules in the *a* state have been recently reviewed in ref. 34. In experiments aimed to detect PA processes as efficiently as possible, non-selective ionization RE2PI schemes are preferred, like those used in ref. 18, 33 and 35 for *a* and *X* state molecules. On the contrary, if quantum state transfer processes are studied, selective detection of molecules distributed among the different ro-vibrational levels is necessary. In the present case we need only to be able to distinguish the electronic state and the vibrational level of the produced molecules so we use selective ionization in the 15 700–16 100 cm^{-1} energy range with the schemes of Fig. 2.

Ionization of deeply bound molecules in the *X* state proceeds *via* the $C^1\Pi_u(6s + 5d)$ state, hereafter referred as *C*, and the $D^1\Sigma_u^+(6s + 5d)$ state, hereafter referred as *D*. Assignment of the observed ionization lines is done according to the known spectroscopy of these states.[36–38] Molecules in the *a* state are ionized *via* the $(3)^3\Sigma_g^+$ excited state. Line assignment is done by calculating the transition energies from ref. 34 and 39 for the *a* and for the $(3)^3\Sigma_g^+$ potential curves, respectively.

Some older spectroscopic data from ref. 33 are also used. In that case $0_g^-(6s + 6p_{1/2})$ lines were simultaneously detected by trap loss and by ion detection (see Fig. 3b). The ionizing laser was tuned in the 14 000 cm^{-1} region, where molecules in both *X* and *a* states are detected. Due to the high density of intermediate states, we consider the detection in this case unselective.

3 Results

Photoassociation as well as photoionization spectra are recorded for all detected $0_g^-(6s + 6p_{1/2})$ levels. This allows us to study both the PA mechanisms and the decay schemes leading to cold molecule formation. In the following, we will

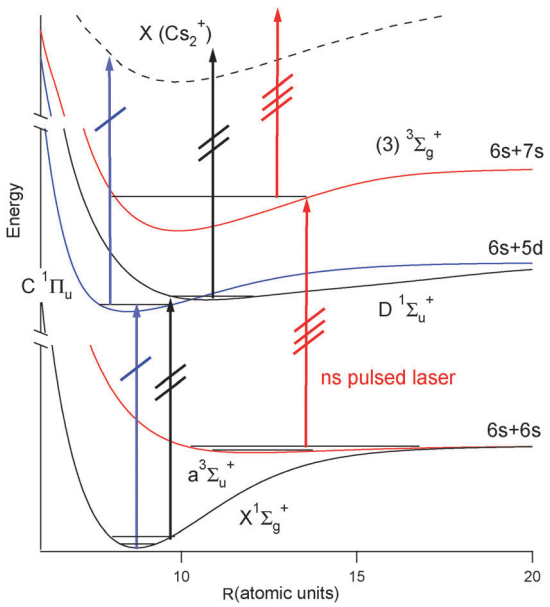

Fig. 2 (color online) The cold molecule detection scheme. Transitions between the *X* – *C* and the *X* – *D* states are used to detect deeply bound *singlet* molecules while transitions between the *a*–$(3)^3\ \Sigma_g^+$ states are used for *triplet* molecules. The energy domain is 15 700–16 100 cm^{-1}. Details are given in the text.

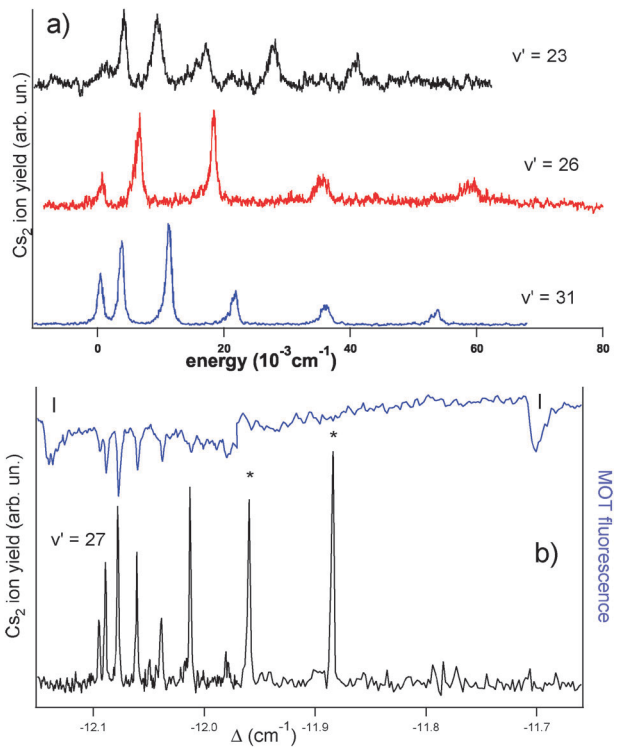

Fig. 3 (color online) (a) Photoassociation spectra for three different vibrational levels of the $0_g^-(6s + 6p_{1/2})$ state. The photoionization laser is adjusted in the 15 700–16 100 cm^{-1} region to the wavelength giving the optimal PA signal for each spectrum. As the PA spectra have been normalized, the different signal to noise ratios are indicative of the different combined formation/detection efficiency for each PA line. (b) Simultaneous recording of ion yield (lower trace) and trap loss (upper trace) for $v' = 27$ (data from ref. 33). Ionization frequency is in the 14 000 cm^{-1} region. Trap loss lines indicated with (I) belong to the $0_u^+(6s + 6p_{1/2})$ series. Lines indicated with (*) are not assigned.

indicate with v the usual vibrational numbering of levels starting from the bottom of the potential curve of each state. On the contrary, the levels of the investigated $0_g^-(6s + 6p_{1/2})$ state will be numbered with the symbol v' which counts the levels starting from the dissociation limit. This is done to be consistent with the following analysis of Section 4. As levels up to dissociation are not all observed, the number of the missing levels is calculated with the LeRoy–Bernstein fit of the vibrational energies of Section 4.1.

3.1 $0_g^-(6s + 6p_{1/2})$ photoassociation spectroscopy

We report in this section the spectroscopic results for the $0_g^-(6s + 6p_{1/2})$ state. The frequencies of the measured lines are summarized in Table 1. It includes some lines ($v' = 11$–18) with an unresolved rotational structure observed by trap loss in ref. 33, some lines ($v' = 20$–27) observed by both trap loss and ion yield and some others ($v' = 28$–44) observed exclusively by ion yield. Two lines, labeled E_1 and E_2, having a particularly large rotational constant are observed. Their position cannot fit into the $0_g^-(6s + 6p_{1/2})$ vibrational progression.

Some PA lines are shown in the spectra of Fig. 3. The observed rotational progression is shown in Fig. 4. Due to our selective detection in the 15 700–16 100 cm^{-1} region we were not able to observe further lines for detunings below 47.5 cm^{-1} with respect to the $6s(F = 4) - 6p_{1/2}(F' = 4)$ transition. Rotational levels from $J = 0$–6 are observed, nevertheless signals of $J = 6$ lines are extremely weak and are not reported in Table 1. The $0_g^-(6s + 6p_{1/2})$ state corresponds to a Hund's case (e) coupling scheme,[31] where the molecular electron angular momentum $\boldsymbol{L}$ and the spin angular momentum $\boldsymbol{S}$ are strongly coupled to each other and to the nuclear rotation angular momentum $\boldsymbol{N}$ (which has quantum number labelled l) but only weakly with the internuclar axis. In this case the good rotational quantum number is $J = l$. As in photoassociation the initial state is a collisional state, l represents also the collisional partial wave. Thus, the observed PA spectra could seem surprising at our atomic temperature of 100 μK because the rotational barrier height for the $l = 6$ partial wave is as

Table 1 Experimental energy detuning Δ and rotational constants B_v of observed lines. Line numbering is given by $v' = \text{integer}(v_D - v)$. The lines $v' = 11$–18 and $E1$, indicated by superscript a, are deduced from older trap loss data.[33] The (negative) detunings Δ are referred to the atomic hyperfine transition $6s(F = 4) - 6p_{1/2}(F' = 4)$ whose absolute energy value 11178.15105 cm^{-1}.[42] For comparison, in the last two columns are reported also the detunings and rotational constants measured at lower resolution in ref. 22. The acronym ND stands for 'not detected'

	Δ detuning/cm^{-1}									
	Present data								Ref. 17	
v'	$J = 0$	$J = 1$	$J = 2$	$J = 3$	$J = 4$	$J = 5$	$1000 \times B_v$	$1000 \times 2\sigma(B_v)$	$J = 1$	$1000 \times B_v$
11			−0.9494[a]							
12			−1.1943[a]							
13			−1.4921[a]							
14	ND									
15			−2.2441[a]						−2.241	
16			−2.7090[a]						−2.704	
17	−3.2443[a]								−3.234	
18			−3.8316[a]						−3.842	
19	ND								ND	
20	−5.2323	−5.2301	−5.2257	−5.2195	−5.2109		1.098	0.005	ND	
21	−6.0427	−6.0401	−6.0353	−6.0282	−6.0189	−6.0067	1.19	0.06	−6.037	
22	−6.9287	−6.9259	−6.9205	−6.9127	−6.9023		1.3	0.1	−6.923	
23	−7.8887	−7.8862	−7.8802	−7.8717	−7.8593	−7.8433	1.51	0.07	−7.875	
24	ND								ND	
25	−9.9558	−9.9520	−9.9426	−9.9280			2.3	0.3	−9.95	1.75
26	−11.0106	−11.0049	−10.9925	−10.9751	−10.9515		2.9	0.1	−11.006	1.78
27	−12.0901	−12.0847	−12.0730	−12.0560	−12.0349	−12.0069	2.77	0.05	−12.086	1.76
28	−13.3053	−13.3015	−13.2916	−13.2781	−13.2610	−13.2385	2.23	0.05	−13.305	2.0
29	−14.6881	−14.6847	−14.6772				1.83	0.05	−14.63	
30	ND									
31	−17.8668	−17.8636	−17.8564	−17.8459	−17.8316	−17.8140	1.76	0.05	−17.865	1.65
32	−19.6366	−19.6332	−19.6259	−19.6152	−19.6010	−19.5833	1.78	0.05	−19.638	1.65
33	−21.5201	−21.5165	−21.5092	−21.4983	−21.4835	−21.4657	1.82	0.05	−21.517	1.84
34	−23.5132	−23.5010	−23.5022	−23.4906	−23.4740	−23.4550	1.94	0.04	−23.682	
35	ND								ND	
36	ND								ND	
37	−30.1231	−30.1180	−30.1074	−30.0921	−30.0716		2.6	0.1	−30.118	2.68
38	−32.3985	−32.3928	−32.3811	−32.3640	−32.3396		2.9	0.1	−32.395	2.8
39	−34.6316	−34.6249	−34.6109	−34.5896	−34.5617	−34.5258	3.53	0.06	−34.626	3.06
40	ND								N.D.	
41	ND								−38.74	
42	−41.7576	−41.7517	−41.7404	−41.7240	−41.7020	−41.6739	2.78	0.05	−41.756	2.6
43	−44.5543	−44.5490	−44.5377	−44.5220	−44.4991	−44.4711	2.77	0.06	−44.551	2.9
44	−47.4569	−47.4508	−47.4387	−47.4212	−47.3982	−47.3676	2.96	0.05	−47.453	2.7
45	ND								−50.498	2.6
E1	−10.4483[a]	−10.3950[a]	−10.3416[a]	−10.2700[a]	−10.2056[a]	−10.1251[a]	8.9[a]	0.1	ND	
E2	−35.9873	−35.9697	−35.9344	−35.8813	−35.8096		8.9	0.1	ND	

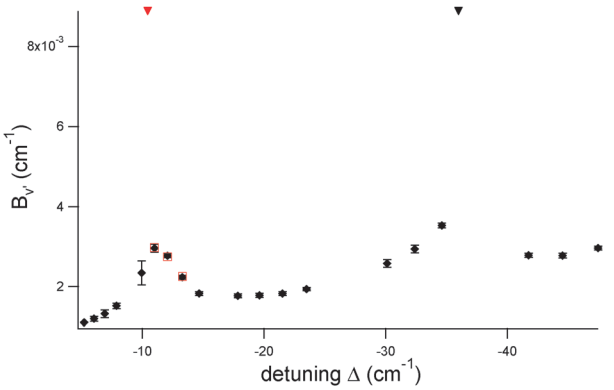

Fig. 4 (color online) Measured rotational constants. Red symbols refer to lines measured in ref. 33. Triangles indicate E1 (red) and E2 (black) lines.

high as 3.5 mK. This is due to the fact that the MOT trapping laser was left on during the PA phase, leading to an acceleration of the colliding pair at long range and thus to an increased number of observed partial waves.[40]

From the trap loss signal of Fig. 3b an estimation of the number of photoassociated (excited) molecules can be obtained. Then, a complete calculation, including transition dipole moments and Frank–Condon factors between all involved levels, would allow us to estimate the number of produced cold ground state molecules. The number of trapped atoms N_{at} in the trap when the PA laser is applied is determined by the rate equation expressing the balance between the loading rate L and the various loss rates

$$\frac{dN_{at}}{dt} = L - \gamma N_{at} - (\beta + \beta_{PA}) \int_{vol} n_{at}^2(r) d^3r \qquad (1)$$

where n_{at} is the atomic density, γ is the loss rate due to background gas collisions, β is the loss rate due to binary collisions among trapped atoms and finally β_{PA} is the loss rate resulting from PA on trapped atoms. The PA rate *per atom* $\mathscr{R}_{PA} = \beta_{PA}\langle n_{at}\rangle$, where $\langle n_{at}\rangle$ is the average atomic density, can be determined from the steady-state solution of eqn (1) which gives for the number N_{PA} ($N_{no\,PA}$) of trapped atoms in presence (absence) of photoassociation

$$\frac{N_{PA}}{N_{no\,PA}} = \frac{\gamma + \beta\langle n_{at}\rangle}{\gamma + (\beta + \beta_{PA})\langle n_{at}\rangle} \qquad (2)$$

considering a Gaussian distribution of the atomic density ($\langle n_{at}\rangle = 2^{-3/2} n_{peak}$, with n_{peak} the peak density) and a uniform intensity of PA laser on the MOT.[33,41] In this case

$$\mathscr{R}_{PA} = (\gamma + \beta\langle n_{at}\rangle)\left(\frac{N_{no\,PA}}{N_{PA}} - 1\right) \qquad (3)$$

Therefore, in the case of ($v' = 27$, $J = 2$) line, where trap losses due to PA amount to 12% of the fluorescence signal and where the no-PA loss rate (*i.e.* in absence of photoassociation) has been separately measured to be $\tau^{-1} = \gamma + \beta\langle n_{at}\rangle = 1.4\ s^{-1}$, we can estimate a PA rate $\mathscr{R}_{PA} \approx 0.2\ s^{-1}$ per atom. For a total number of trapped atoms $N_{at} = 5 \times 10^7$, this gives a rate of 5×10^6 photoassociated (excited) molecules per second.

To calculate the ground state molecular yield for this line we should evaluate the branching ratio between the spontaneous decay into two free atoms and that into a bound molecule. As discussed, the latter is possible either *via* a direct decay into the a state or *via* the two-step cascade decay into the X state through the intermediate 0_u^+ state. As the second process can proceed through a large number of intermediate vibrational levels, the exact calculation is quite lengthy and has not been performed here. Therefore we propose here a simple estimate of the number of produced molecules instead. The relatively large ($\sim$40) number of detected ions per shot with an estimated microchannel-plate detection efficiency of 10% allows us to say that the production rate is larger than 400 molecules in the 10 ms of molecular residence time in the detection region. The maximum molecular yield would be obtained when all the photoexcited molecules decay into ground state molecules, *i.e.* 5×10^4 molecules in 10 ms. We expect the real yield to be in between these two numbers, probably closer to the upper limit as the rotational constant of this line corresponds to a wavefunction with an average distance $\langle R\rangle = 18.2a_0$, a_0 being the Bohr radius, short enough to decay mainly towards the bound levels of the a and X states.

3.2 Production of deeply bound molecules in the X state

Fig. 5d shows the photoionization (PI) spectrum obtained, for reference, with the PA laser tuned to the $v = 6$ of the upper $0_g^-(6s + 6p_{3/2})$ state at 11665.2055 cm^{-1}, following the level numbering of ref. 43. In this case the PA process populates many vibrational levels in the a state. All the visible PI lines can be assigned to a-$(3)^3\Sigma_g^+$ transitions. No triplet molecules are efficiently detected for ionization energies in the region immediately below 15827.5 cm^{-1}. We notice incidentally that, at our lower resolution, we can fully confirm the energy level spacings for the a state that can be calculated from the potential curve deduced in ref. 39 (red, black and blue lines below Fig. 5d). The PI spectra in Fig. 5a show that the first detected levels ($v' = 23$ in the figure) of the $0_g^-(6s + 6p_{1/2})$

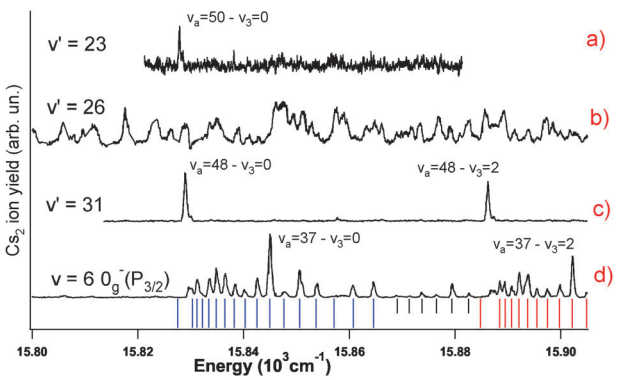

Fig. 5 (color online) Photoionization spectra for different PA lines. In (a), (b) and (c) the PA laser is tuned to the $J = 2$ ro-vibrational line of the $v' = 23$, 26 and 31 vibrational levels of the $0_g^-(6s + 6p_{1/2})$ state, respectively. The (d) spectrum is taken with the PA laser tuned to the $v = 6$, $J = 2$ ro-vibrational level of the upper $0_g^-(6s + 6p_{3/2})$ state. Red (black, blue) lines correspond to calculated transition energies between vibrational levels v_a of the a state and of the $v_3 = 0$ ($v_3 = 1, 2$) level of the $(3)^3\Sigma_g^+$ excited state.

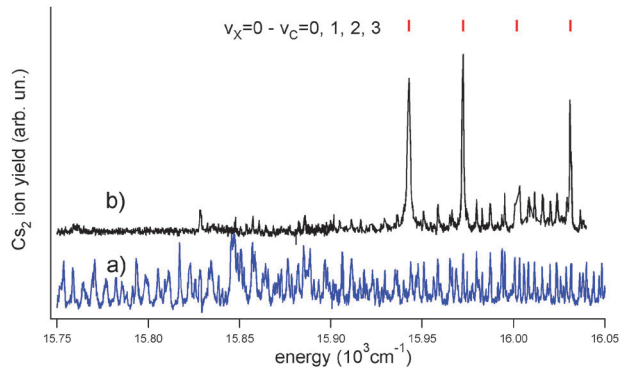

Fig. 6 (color online) Photoionization spectra for the $v' = 26$, $J = 2$ PA line, without (a) and with (b) a vibrational pumping phase, respectively. The vertical scale is the same for the two spectra and a constant 20 ion offset is added to the (b) curve for clarity.

state close to dissociation produce cold molecules in mainly one or two of the highest vibrational levels ($v_a = 50$ in this case) of the a state. Exciting the more deeply bound 0_g^- levels ($v' = 25$–29), PI spectra change: the intensity of the lines coming from a levels decreases while new lines, not corresponding to any known a state transition, appear. At some point (see Fig. 5b) the spectrum becomes very dense. Nevertheless, it can be completely interpreted as composed of several transitions between deeply bound levels ($v_X = 0$–60) of the X state and excited levels belonging to the C and D states and by transitions between deeply bound levels ($v_a = 6$–18) of the a state and excited levels belonging to the $(3)^3\Sigma_g^+$ state.

As detuning is further increased ($v' = 31$–34), PI spectra become again essentially composed of lines coming from ionization of high lying vibrational levels ($v_a \approx 48$) of the a state (see Fig. 5c). A second region of modified decay towards the X state is observed for levels around detuning $\Delta \approx -35$ cm^{-1} ($v' = 38$–39).

In addition to the spectroscopic assignment, by applying a vibrational pumping phase during molecule formation we demonstrate that the decay products of the PA lines for detunings around -11 cm^{-1} and -35 cm^{-1} belong to the X state. This experimental procedure consists of illuminating the sample with a series of pulses of a mode-locked femtosecond laser whose spectrum has been modified in order to eliminate all molecular transitions starting from the $v_X = 0$ level.[7] In this way, a large fraction of the molecules originally in the $v_X = 1$–60 levels are optically pumped into the $v_X = 0$ level (the rest is pumped towards higher vibrational levels ($v_X > 60$) that are not detected). Molecules in any level of the a state are not affected by the pumping process at this wavelength. The same result can be obtained by using a shaped broadband diode laser.[29] The result is shown in Fig. 6. After applying the vibrational pumping phase there is a clear accumulation of molecules into the $v_X = 0$ level (Fig. 6b) together with a depletion of most other lines of the spectrum. The remaining lines can be assigned to transitions originating from deeply bound levels ($v_a = 6$–18) of the a state. This demonstrates that, following PA of $0_g^-(6s + 6p_{1/2})$ levels in the -11 cm^{-1} and -35 cm^{-1} detuning region, a large fraction of ground state molecules are produced either by one-photon decay into deeply bound levels of the a state, that were not populated before, or by two-photon decay into deeply bound levels ($v_X = 0$–60) of the ground X state.

To precisely determine the populations in the different levels of the a and X states we fitted our experimental ion signal. The fitting model considers all the experimental (a – (3), X – C and X – D) transition energies in the explored PI domain, the experimental (when available) or computed dipole moments and FC factors for the intermediate ionization step, and a uniform ionization rate for the second step into the Cs_2^+ continuum. The results, corresponding to spectra in Fig 5 and 6, are shown in Fig 7. Considering the uncertainty of the calculated FC factors used in the fit the results should be considered as an estimate of the population distributions. Nevertheless, firstly Fig. 7a clearly shows that the PA in the perturbed region produces population in deeply bound ($v_a = 5$–18) levels of the a state that are not at all present after PA of unperturbed 0_g^- levels. Moreover, due to the limited extension in the blue side of the ionization spectrum, we are not probing the molecular population in the first 7 levels ($v_a = 0$–6). Secondly, Fig. 7b shows that a large fraction of the population in the first 60 vibrational levels of the X state are optically pumped into the single $v_X = 0$ level. Finally, we observe that the number of molecules in the a state largely exceeds that in the X state. Even if these numbers, and thus their branching ratio, suffer from the incertitudes discussed above, it is clear that the direct two-photon decay into the X state is not the leading process. This renews the interest for an optical pumping process capable of converting *triplet* ground state molecules into *singlet* ones.[27,28]

4 Analysis using the vibrational quantum defect

The method of analysis consists of converting the binding energy, ε, of each vibrational level (v, $J = 0$) into a number

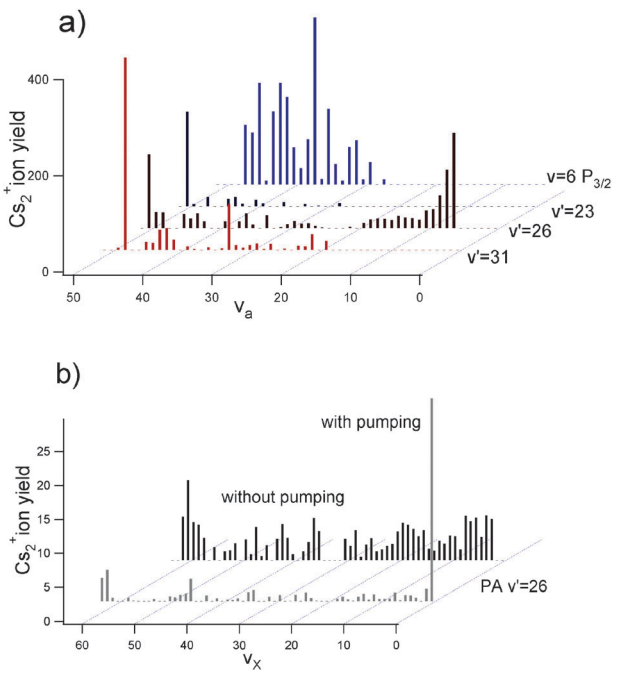

Fig. 7 (color online) Fitted populations of cold molecules in different vibrational levels of the a state (a), corresponding to spectra shown in Fig. 5, and of the X state (b), corresponding to spectra of Fig. 6.

denoted δ, which is the vibrational quantum defect (VQD). The conversion is done *via* an assumed energy law. In our case the energy law is the LeRoy–Bernstein (LRB) one,[44,45] which gives the eigenvalues of the $-c_6/R^6$ potential curve. The VQD δ is then plotted *versus* the binding energy ε for a series of vibrational levels. δ is defined in such a way that if the set of data satisfies the assumed law, then δ is constant. To show the discrepancies, δ is plotted *versus* the binding energy ε for all the set of data. The obtained (ε, δ) graph is similar to the well-known Lu–Fano graph.[46] If the assumed law is satisfied the expected (ε, δ) graph is a horizontal line. If not, the (ε, δ) graph exhibits perturbations in the level series, generally due to a coupling which is not included in the simple assumed law. The next step consists of proposing a coupling model, for example two coupled series, in order to extract an estimate of the coupling strength and the characteristics of each series.

Such a method has already been applied successfully to spectroscopic data of long range molecules of rubidium[26,47] and caesium[24,48] dimers.

Up to now one observed two types of (ε, δ) graphs. In the case of the $0_g^-(5s + 5p_{1/2})$ series of Rb_2,[26] the (ε, δ) graph was linear. The slope was interpreted as a short range effect in the molecular potential which was ignored in the 1970 LRB model.[44] An improvement of the LRB law has confirmed this linear additional term.[49,50]

In the case of the $0_u^+(5s + 5p_{1/2})$ series of Rb_2,[47] $0_u^+(6s - 6p_{1/2})$ series of Cs_2[48] and an earlier study of the Cs_2 $0_g^-(6s - 6p_{1/2})$ series[24] the (ε, δ) graph was linear with additional sudden sharp variations. These variations were interpreted as local perturbations of the molecular levels due to a coupling with a neighboring vibrational series, having nearly resonant levels.

4.1 LeRoy–Bernstein formula

Details about the LRB formula, the method to obtain it and its validity, are given in Section 2 of ref. 24. The LRB formula gives the binding energy ε of eigenstates for a potential curve expressed as $-c_n/R^n$. If v denotes the number of the level (vibrational number) then ε is

$$\varepsilon = E_n (v_D - v)^{2n/(n-2)} \qquad (4)$$

In this formula, v_D is a constant whose integer part gives the number of states in the potential and E_n is an energy value related to the reduced mass and to c_n. The general expression of E_n is given in ref. 24, 44 and 45.

The asymptotic potential of the Cs_2 $0_g^-(6s + 6p_{1/2})$ state, expressed in the Hund's case (c) basis, is given by $-c_6/R^6$ where—due to the change of basis, from Hund's case (a) to Hund's case (c)—the effective coefficient c_6 involves the C_3, C_6^Π and C_6^Σ coefficients. The expression of c_6 and the values for C_3, C_6^Π and C_6^Σ taken from ref. 51 and other literature, are discussed in detail in ref. 24 and 48. Here we pick out the main established result, namely $c_6 = (9.3732 \pm 0.0229) \times 10^5$ au giving $E_6 = (6.8825 \pm 0.0084) \times 10^{-4}$ cm^{-1}.

4.2 Effective vibrational number and VQD

In the analysis using the VQD, the LRB formula is applied to define the *effective* non-integer vibrational quantum number, $v^* = v_D - v$, of the measured level with the binding energy ε. For each measured vibrational level of the $0_g^-(6s + 6p_{1/2})$ potential curve having $n = 6$, v^* is defined as

$$v^* = (\varepsilon/E_6)^{1/3}$$

The VQDs are defined as

$$\delta = v^* - \text{Integer}[v^*]$$

It is straightforward to see that if the LRB formula is satisfied by a series of levels, then $\delta = v_D - \text{Integer}[v_D] = \text{constant}$ for all the levels. Thus the (ε, δ) graph would be a horizontal line.

Applying the method to the $J = 0$ data of Table 1, we obtain the (ε, δ) graph given in Fig. 8. The (ε, δ) graph exhibits two perturbations located close to 11 cm^{-1} and 35 cm^{-1} as it was observed in ref. 24. These locations are in agreement with the resonances of the rotational constant which are clearly visible in the (ε, B_v) graph of Fig. 4. The last point in Fig. 8, which has been excluded from the following fit, would appear close to the fitted curve if negative values of VQD were allowed. This discrepancy is probably due the limited accuracy of the c_6 and E_6 values used in the assumed law of eqn (4).

4.3 Analysis using a two-series model

As done in ref. 24, the (ε, δ) graph is analyzed using a two-series model. The procedure starts with the Demkov and Ostrovsky model,[52] where the two considered series have regularly spaced levels (spacings Δ_1 and Δ_2) coupled *via* an assumed constant coupling V. In this case, the solutions for the eigenenergy ε are given by

$$\tan\left[\pi\frac{\varepsilon-\varepsilon_1}{\Delta_1}\right] \times \tan\left[\pi\frac{\varepsilon-\varepsilon_2}{\Delta_2}\right] = \pi^2 K^2 \qquad (5)$$

where ε_1 (respectively ε_2) is one of the unperturbed levels of series 1 (resp. series 2) and K the reduced coupling defined by $K^2 = \frac{V^2}{\Delta_1\Delta_2}$.

To be applied to coupled molecular series, with non regularly spaced levels, the model has been adapted. In the case of a series following the LRB energy law, the pertinent quantity is v^* which is regularly spaced (the spacing is 1). It leads to the transformation of $\tan[\pi\frac{\varepsilon-\varepsilon_1}{\Delta_1}]$ to $\tan[\pi(v^* - v_1^*)]$. Because of its definition, the VQD δ is also a pertinent quantity.

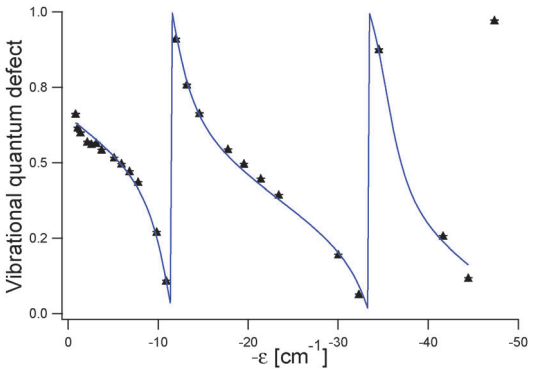

Fig. 8 (color online) Experimental vibrational quantum defects (black dots) fitted by eqn (6) (solid line). The last point, whose quantum defect is close to one, has been excluded from the fit.

In the considered energy region, the $0_g^-(6s + 6p_{1/2})$ series can be described by the LRB model. For the perturbing state (supposed here to be the $0_g^-(6s + 6p_{3/2})$ one) only two levels are involved. The spacing between them is denoted Δ_2. For that reason we consider the coupling of a LRB series with a regular one and we use the following equation

$$\tan[\pi(\delta - \mu)] \times \tan\left[\pi\frac{\varepsilon - \varepsilon_2}{\Delta_2}\right] = \pi^2 K^2 \qquad (6)$$

to fit the plot of Fig. 4. The quantity μ is the VQD of a unperturbed level of the series 1. To include the linear additional term in the LRB formula,[24,49] as mentioned above, we also impose a linear variation of the VQD by taking $\mu = \mu_0 - \gamma\varepsilon$. Because the experimental data set is narrow, the second series is limited to two levels separated by Δ_2 with one of them located at ε_2.

The fitting procedure, shown by the blue line in Fig. 8, provides the following values: $\mu_0 = 0.66 \pm 0.01$; $\gamma = 0.0119 \pm 0.0005$; $\varepsilon_2 = 11.424 \pm 0.114$ cm^{-1}; $\Delta_2 = 23.914 \pm 0.243$ cm^{-1}; and $K = 0.1652 \pm 0.0047$. These values are in agreement with results of ref. 24.

4.4 Wavefunction mixing and rotational constant estimation

The fitting parameters are then used to construct the matrix of the unperturbed levels plus the coupling values. The unperturbed levels of the LRB series are defined by $v^* = (\varepsilon_i/E_6)^{1/3} = i + \mu_0 - \gamma\varepsilon_i$ for $i = 11$ to 45. The two levels of the series 2 are located at ε_2 and $\varepsilon_2 + \Delta_2$. Including the coupling V the total matrix is then diagonalized giving the eigenvalues and the wavefunctions. The mixing coefficient (the character of the level ε_2 or $\varepsilon_2 + \Delta_2$ in the eigenfunction) is denoted α and its squared value is shown in Fig. 9. A mixing up to 30 percent is observed at a binding energy close to 35 cm^{-1} which explains the enhancement in the molecule formation at this energy value.

The wavefunction mixing is also used to evaluate the rotational constant B_v in order to compare to experimental data of Fig. 4. We first consider the analytic expression of the rotational constant given by LeRoy in 1972.[53] For a $-c_6/R^6$ potential, the rotational constant is $B_v^{LR} = B_{v6}(v_D - v)$ where

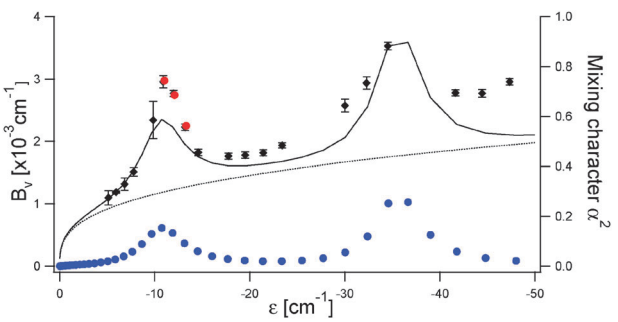

Fig. 9 (color online) Left axis: comparison between experimental and deduced rotational constants. Black dots: experimental B_v, dotted line: unperturbed values B_v^{LR} after eqn (7), solid line: perturbed values B_v^{VQD} given by eqn (8). Right axis (blue dots): weight α^2 of the second series character in the perturbed wavefunctions.

$B_{v6} = \frac{3}{8\pi^2}\frac{\Gamma(2/3)\Gamma(1/3)}{\Gamma(1/6)\Gamma(5/6)}E_6$. Then, we deduce

$$B_v^{LR}(\varepsilon) = B_{v6}\left(\frac{\varepsilon}{E_6}\right)^{1/3} \qquad (7)$$

With the E_6 value given previously, we obtain $B_{v6} \simeq 4.74 \times 10^{-5}$ cm^{-1} and plot this formula in Fig. 9 (dotted line).

Due to the coupling, the deduced rotational constant B_v^{VQD} is a combination of $B_v^{LR}(\varepsilon)$ and of the rotational constant B_v^{pert} of the perturbing series. It is written as‡

$$B_v^{VQD}(\varepsilon) = (1 - \alpha^2)B_v^{LR}(\varepsilon) + \alpha^2 B_v^{pert} \qquad (8)$$

Using the mixing α^2 of Fig. 9, and the value $B_v^{pert} = 0.0088$ cm^{-1} computed from the adiabatic $0_g^-(6s + 6p_{3/2})$ of Fig. 1, we deduce the plot of Fig. 9 (solid line). This curve, which is not a fitting one, is in good agreement with the experimental B_v values. The discrepencies, which are less of 25 percent, are probably mainly due to the LRB model[53] which neglects the short range potential effects.

5 Theoretical model

As stated in the previous section, the irregular variation of the rotational constants of the PA lines is a well-known manifestation of the population of rovibrational levels of coupled electronic states, as first observed in our group in the cold molecule context in ref. 15. The sudden increase of the rotational constant for isolated lines suggests that deeply-bound energy levels (*i.e.* with a vibrational motion mainly localized at short internuclear distance R) are populated starting from a PA level essentially populated at large R.

Like in our previous papers, we looked for possible interactions between electronic states giving rise to resonant coupling between related weakly-bound and deeply-bound levels. Fig. 10 displays the relevant excited electronic states in the Hund's case (a) representation, which result into the 0_g^- states represented in Fig. 1. These potential curves are obtained from calculations according to the method of ref. 54. Note that the $(2)^3\Sigma_g^+$ curve has been shifted upward by 214 cm^{-1} following ref. 34. The $(1)^3\Sigma_g^+$ and $(1)^3\Pi_g$ states (with potential curves $V_{(1)}(R)$ and $V_\Pi(R)$) are coupled by spin–orbit interaction, resulting into two 0_g^- states correlated to the $6s_{1/2} + 6p_{1/2,3/2}$ asymptotes. Weakly-bound levels of the $0_g^-(6s + 6p_{1/2})$ state are initially populated by PA in the present experiment. The $0_g^-(6s + 6p_{3/2})$ state has a double-well potential which gave rise to the first observation of ultracold molecules.[35] In addition the $(2)^3\Sigma_g^+$ potential curve $V_{(2)}$ (R) correlated to the 6s + 5d limit is deep enough to have a minimum in the energy range of the $(1)^3\Sigma_g^+$ and $(1)^3\Pi_g$ wells. The crossing between the $(1)^3\Pi_g$ and the $(2)^3\Sigma_g^+$ curves is responsible for giant resonant lines analyzed in our previous experiments.[14,56] As indicated in Fig. 10a the $(1)^3\Sigma_g^+$ and $(2)^3\Sigma_g^+$ curves also undergo an avoided crossing around $8a_0$ in the region of their inner wall. This feature is confirmed by the R variation of the transition dipole moment (TDM) functions (Fig. 10c), where the $(1)^3\Sigma_g^+$-$a^3\Sigma_u^+$ and $(2)^3\Sigma_g^+$-$a^3\Sigma_u^+$

‡ The wavefunction written as $\psi = \alpha\psi(\varepsilon_2) + \Sigma\beta_i\psi(\varepsilon_i)$ allows to express $B_v = \langle\psi|\hbar^2/(2\mu R^2)|\psi\rangle$ as $B_v \approx \alpha^2 B_v(\varepsilon_2) + (1 - \alpha^2)B_v^{LR}(\varepsilon)$ because the crossed terms as $\langle\psi|(\varepsilon_2)|\hbar^2/(2\mu R^2)|\psi(\varepsilon_i)\rangle$ are negligible.

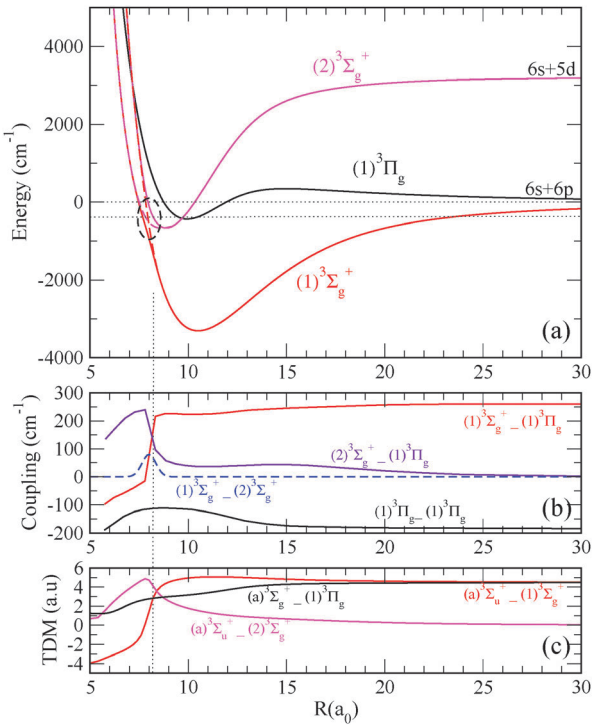

Fig. 10 (a) Potential curves relevant for the present cold molecule formation process, calculated after ref. 54. The avoided crossing between the $(1)^3\Sigma_g^+$ and $(2)^3\Sigma_g^+$ curves is indicated with a circle, and the position of the $6s_{1/2} + 6p_{1/2}$ asymptote with the lowest dotted line. (b) Corresponding spin–orbit couplings $W^{so}(R)$ (full lines) (ref. 55) and radial coupling $W^{rad}(R)$ (dashed line). (c) Transition dipole moments between the *a* state and the three states of panel (a).

TDM cross each other around $8a_0$ meaning that both states exchange their character at the avoided crossing.

We model the problem by setting up a three-state electronic hamiltonian H^{so}_{diab}:

$$H^{so}_{diab} = \begin{pmatrix} V_{\Pi}(R) + W^{so}_{\Pi}(R) & W^{so}_{\Pi-(1)}(R) & W^{so}_{\Pi-(2)}(R) \\ W^{so}_{\Pi-(1)}(R) & V_{(1)}(R) & W^{rad}(R) \\ W^{so}_{\Pi-(2)}(R) & W^{rad}(R) & V_{(2)}(R) \end{pmatrix} \quad (9)$$

where $W^{so}_{\Pi}(R)$ is the diagonal spin–orbit shift of the $(1)^3\Pi_g$ state, and $W^{so}_{\Pi-(1)}(R)$ and $W^{so}_{\Pi-(2)}(R)$ the off-diagonal spin–orbit couplings between the $(1)^3\Pi_g$ and the $(1)^3\Sigma_g^+$ and $(2)^3\Sigma_g^+$ state, respectively[55] (Fig. 10b). Note that these two functions cross each other around $8a_0$ confirming the interaction between the two $^3\Sigma_g^+$ states. The main parameter of the model $W^{rad}(R)$ is taken as a Gaussian function $W^{rad}(R) = W_0 \exp(-(R - R_0)^2/\Delta r)$ localized at $R_0 = 8a_0$ (Fig. 10b).

Neglecting rotation and hyperfine effects, we computed the vibrational energies and wave functions of the three-coupled state system with the Mapped Fourier Grid Hamiltonian (MFGH) method.[57] A useful way to display the results consists in representing the rotational constant of the eigenstates as a function of their binding energy. In Fig. 11 we compare these results to those of a two-state model involving $(1)^3\Pi_g$ and $(1)^3\Sigma_g^+$. The latter model shows two distinct series of rotational constants related to the 0_g^- potential curves

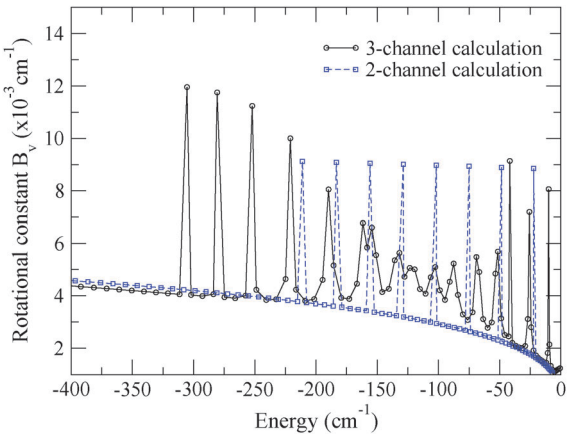

Fig. 11 Rotational constants B_v of the 0_g^- levels for a two-coupled state model involving $(1)^3\Pi_g^+$ and $(1)^3\Sigma_g^+$ (open squares), and for a three-coupled state ($(1)^3\Pi_g$, $(1)^3\Sigma_g^+$, $(2)^3\Sigma_g^+$) model (open circles). Lines are drawn to guide the eye. The origin of energies is taken at the $6s_{1/2} + 6p_{1/2}$ limit.

obtained after the diagonalization of the corresponding 2×2 submatrix in H^{so}_{diab}. They correspond to two vibrational series associated to the $0_g^-(6s + 6p_{1/2})$ and $0_g^-(6s + 6p_{3/2})$ with no mutual interaction. We checked that the eigenstates have a pure $0_g^-(6s + 6p_{1/2})$ (lower series of B_v values) or $0_g^-(6s + 6p_{3/2})$ (upper series of B_v values, starting around -220 cm^{-1}) character. Therefore this coupling cannot be responsible for the population of short-range $0_g^-(6s + 6p_{3/2})$ vibrational levels after PA of long-range $0_g^-(6s + 6p_{1/2})$ levels.

The three-channel model provides a spectacular change. A new series of levels with large B_v appears around -305 cm^{-1}, corresponding to the lowest levels of the $0_g^-((2)^3\Sigma_g^+)$ state. This series is soon perturbed when entering the energy range of the avoided crossing with the $(1)^3\Sigma_g^+$, modifying in turn all wave functions of the $0_g^-(6s + 6p_{1/2})$ and $0_g^-(6s + 6p_{3/2})$ levels. We zoomed these results on the experimental energy range (Fig. 12). We clearly see that many levels have irregular B_v values (around -10 cm^{-1}, between -30 and -20 cm^{-1}, and between -55 and -45 cm^{-1}) which manifest strong wave function mixing. We observe a qualitative agreement with the features observed in

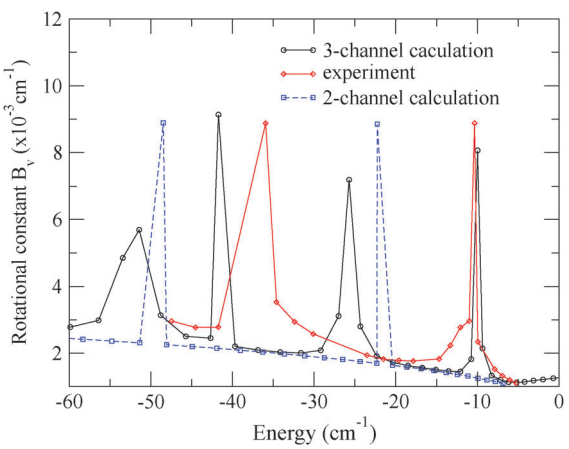

Fig. 12 Zoom of Fig. 11 in the region of the experimental results (open diamonds).

Fig. 4 of the experiment, while the magnitude of B_v is in good agreement. Both the position of the perturbed energy levels and the amplitude of the wave function mixing cannot be exactly predicted from the model, which relies on *ab initio* potential curves and couplings. Nevertheless the necessity to include the $(2)^3\Sigma_g^+$ state to induce the coupling between $0_g^-(6s + 6p_{1/2})$ levels populated by PA at long-range with short-range levels is clearly demonstrated. The eigenstates of the three patterns in the above regions have wavefunctions equally spread over the three electronic states, while those with the largest rotational constant correspond to almost pure $0_g^-(6s + 6p_{3/2})$ levels slightly mixed with the $(2)^3\Sigma_g^+$ state. A deeper analysis of this process is currently in progress, involving the quite large flexibility of the parameters due to the limited accuracy of the theoretical potential curves. A more extensive investigation by conventional spectroscopy of these states would be desirable to identify the exact location of these perturbations, in order to extract potential curves for all internuclear distances.

6 Conclusions

In this paper we performed a *complete* photoassociation experiment by exciting, in a limited range below the $6s + 6p_{1/2}$ molecular asymptote, the 0_g^- state in a cold caesium sample and by selectively detecting the molecular decay products. The recorded progressions of vibrational and rotational levels showed strong perturbations for two PA energy domains, at detunings around $\Delta = -11$ cm^{-1} and -35 cm^{-1}. These perturbations have been analyzed in terms of quantum defects, allowing us to determine the positions of the two perturbing molecular levels and the mixing of the molecular wavefunctions. A theoretical model involving the resonant coupling of the investigated 0_g^- state with two upper 0_g^- states connected to the $6s + 6p_{3/2}$ and $6s + 5d$ asymptotes has been necessary to explain the appearence of such strong perturbations in the spectroscopic signature of the state.

Moreover, a selective analysis of the decay products of the PA process allowed the monitoring of the change in the population distribution of produced cold ground state molecules. While PA in unperturbed 0_g^- levels ends up mainly in the very highest vibrational levels of the a state, the resonant coupling enhances short range character of the excited molecules allowing a one-photon decay into the deepest bound levels ($v_a = 6$–18) of the a state and a two-photon decay into many deeply bound levels of the X state. The latter one can be efficiently optically pumped into the single $v_X = 0$ level.

This experiment, using the richness of the caesium molecule in terms of couplings, allows for the identification and for the characterization of both an excitation and a decay step that efficiently produce cold molecules in deeply bound levels. These mechanisms, in particular the two photon decay, should appear ubiquitously in other homonuclear and heteronuclear systems. They could be used to engineer schemes for cold molecule production and quantum population transfer. Finally, although an important fraction of the molecules can be put into the $v_X = 0$ level, the largest part of cold molecules are spread over a relatively large number of levels of the a state. It would be very important to find a way to transfer population between these two electronic states. In this direction, a theoretical study has been already published[28] and an experiment is in progress in our laboratory.[27] The ensemble of studies pave the way towards a complete control of both translational and internal degrees of freedom of simple molecular systems and to applications.

This work is supported by the "Institut Francilien de Recherche sur les Atomes Froids" (IFRAF). This work is also partially supported by the network "Quantum Dipolar Molecules (QuDipMol)" of the EUROQUAM framework of the European Science Foundation (ESF). A.F. has been supported by the "*Triangle de la Physique*" under contracts 2007-n.74T and 2009-035T "GULFSTREAM". M.A. thanks the EC-Network EMALI, the "*Université Franco-Italienne*" (Galileo Project) and the bilateral project between the University of Paris-Sud and the University of Pisa.

References

1 I. W. M. Smith, *Low Temperatures and Cold Molecules*, Imperial College Press, 2008.
2 R. V. Krems, W. C. Stwalley and B. Friedrich, *Cold Molecules, Theory, Experiment, Applications*, CRC Press, 2009.
3 O. Dulieu and C. Gabbanini, *Rep. Prog. Phys.*, 2009, **72**, 086401.
4 L. D. Carr and J. Ye, *New J. Phys.*, 2009, **11**, 055009.
5 A. N. Nikolov, E. E. Eyler, X. T. Wang, J. Li, H. Wang, W. C. Stwalley and P. L. Gould, *Phys. Rev. Lett.*, 1999, **82**, 703–706.
6 J. Deiglmayr, A. Grochola, M. Repp, K. Mörtlbauer, C. Glück, J. Lange, O. Dulieu, R. Wester and M. Weidemüller, *Phys. Rev. Lett.*, 2008, **101**, 133004.
7 M. Viteau, A. Chotia, M. Allegrini, N. Bouloufa, O. Dulieu, D. Comparat and P. Pillet, *Science*, 2008, **321**, 232.
8 D. Sofikitis, S. Weber, A. Fioretti, R. Horchani, M. Allegrini, B. Chatel, D. Comparat and P. Pillet, *New J. Phys.*, 2009, **11**, 055037.
9 K. Aikawa, D. Akamatsu, M. Hayashi, K. Oasa, J. Kobayashi, P. Naidon, T. Kishimoto, M. Ueda and S. Inouye, *Phys. Rev. Lett.*, 2010, **105**, 203001.
10 K.-K. Ni, S. Ospelkaus, M. H. G. de Miranda, A. Pe'er, B. Neyenhuis, J. J. Zirbel, S. Kotochigova, P. S. Julienne, D. S. Jin and J. Ye, *Science*, 2008, **322**, 231.
11 J. G. Danzl, M. J. Mark, E. Haller, M. Gustavsson, R. Hart, J. Aldegunde, J. M. Hutson and H.-C. Nägerl, *Nat. Phys.*, 2010, **6**, 265.
12 W. Demtröder, *Molecular Physics*, Wyley-VCH, 2005.
13 C. Amiot, O. Dulieu and J. Vergès, *Phys. Rev. Lett.*, 1999, **83**, 2316–2319.
14 M. Vatasescu, C. M. Dion and O. Dulieu, *J. Phys. B: At., Mol. Opt. Phys.*, 2006, **39**, S945.
15 C. M. Dion, C. Drag, O. Dulieu, B. Laburthe Tolra, F. Masnou-Seeuws and P. Pillet, *Phys. Rev. Lett.*, 2001, **86**, 2253–2256.
16 A. Fioretti, O. Dulieu and C. Gabbanini, *J. Phys. B: At., Mol. Opt. Phys.*, 2007, **40**, 3283.
17 H. K. Pechkis, D. Wang, Y. Huang, E. E. Eyler, P. L. Gould, W. C. Stwalley and C. P. Koch, *Phys. Rev. A: At., Mol., Opt. Phys.*, 2007, **76**, 022504.
18 M. Viteau, A. Chotia, M. Allegrini, N. Bouloufa, O. Dulieu, D. Comparat and P. Pillet, *Phys. Rev. A: At., Mol., Opt. Phys.*, 2009, **79**, 021402.
19 B. E. Londoño, J. E. Mahecha, E. Luc-Koenig and A. Crubellier, *Phys. Rev. A: At., Mol., Opt. Phys.*, 2009, **80**, 032511.
20 W. C. Stwalley, J. Banerjee, M. Bellos, R. Carollo, M. Recore and M. Mastroianni, *J. Phys. Chem. A*, 2010, **114**, 81–86.
21 J. M. Sage, S. Sainis, T. Bergeman and D. DeMille, *Phys. Rev. Lett.*, 2005, **94**, 203001-1–203001-4.
22 M. Pichler, H. Chen and W. C. Stwalley, *J. Chem. Phys.*, 2004, **121**, 1796.
23 M. Pichler, W. C. Stwalley and O. Dulieu, *J. Phys. B: At., Mol. Opt. Phys.*, 2006, **39**, S981.
24 L. Pruvost and H. Jelassi, *J. Phys. B: At., Mol. Opt. Phys.*, 2010, **43**, 125301.
25 V. Kokoouline, C. Drag, P. Pillet and F. Masnou-Seeuws, *Phys. Rev. A: At., Mol., Opt. Phys.*, 2002, **65**, 062710.

26 H. Jelassi, B. Viaris de Lesegno and L. Pruvost, *Phys. Rev. A: At., Mol., Opt. Phys.*, 2006, **73**, 032501.
27 R. Horchani, H. Lignier, N. Bouloufa, A. Fioretti, P. Pillet and D. Comparat, in preparation, 2011.
28 N. Bouloufa, M. Pichler, M. Aymar and O. Dulieu, *Phys. Rev. A: At., Mol., Opt. Phys.*, 2011, **83**, 022503.
29 D. Sofikitis, R. Horchani, X. Li, M. Pichler, M. Allegrini, A. Fioretti, D. Comparat and P. Pillet, *Phys. Rev. A: At., Mol., Opt. Phys.*, 2009, **80**, 051401.
30 D. Sofikitis, A. Fioretti, S. Weber, R. Horchani, M. Pichler, X. Li, M. Allegrini, B. Chatel, D. Comparat and P. Pillet, *Mol. Phys.*, 2010, **108**, 795–810.
31 K. M. Jones, E. Tiesinga, P. D. Lett and P. S. Julienne, *Rev. Mod. Phys.*, 2006, **78**, 483–535.
32 N. Vanhaecke, C. Lisdat, B. T'Jampens, D. Comparat, A. Crubellier and P. Pillet, *Eur. Phys. J. D*, 2004, **28**, 351.
33 C. Drag, *PhD thesis*, Université Paris XI Orsay, 2000.
34 N. Bouloufa, E. Favilla, M. Viteau, A. Chotia, A. Fioretti, C. Gabbanini, M. Allegrini, M. Aymar, D. Comparat, O. Dulieu and P. Pillet, *Mol. Phys.*, 2010, **108**, 2355–2368.
35 A. Fioretti, D. Comparat, A. Crubellier, O. Dulieu, F. Masnou-Seeuws and P. Pillet, *Phys. Rev. Lett.*, 1998, **80**, 4402–4405.
36 M. Raab, G. Höning, W. Demtröder and C. R. Vidal, *J. Chem. Phys.*, 1982, **76**, 4370–4386.
37 C. Amiot, W. Demtröder and C. R. Vidal, *J. Chem. Phys.*, 1988, **88**, 5265–5281.
38 H. Katô, T. Kobayashi, M. Chosa, T. Nakahori, T. Iida, S. Kasahara and M. Baba, *J. Chem. Phys.*, 1991, **94**, 2600–2607.
39 F. Xie, V. B. Sovkov, A. M. Lyyra, D. Li, S. Ingram, J. Bai, V. S. Ivanov, S. Magnier and L. Li, *J. Chem. Phys.*, 2009, **130**, 051102.
40 A. Fioretti, D. Comparat, C. Drag, T. F. Gallagher and P. Pillet, *Phys. Rev. Lett.*, 1999, **82**, 1839–1842.
41 C. Drag, B. Tolra, O. Dulieu, D. Comparat, M. Vatasescu, S. Boussen, S. Guibal, A. Crubellier and P. Pillet, *IEEE J. Quantum Electron.*, 2000, **36**, 1378–1388.
42 D. Steck, *Cesium D Line Data*, Available online at http://steck.us/alkalidata, 2008.
43 A. Fioretti, D. Comparat, C. Drag, C. Amiot, O. Dulieu, F. Masnou-Seeuws and P. Pillet, *Eur. Phys. J. D*, 1999, **5**, 389–403.
44 R. J. LeRoy and R. B. Bernstein, *J. Chem. Phys.*, 1970, **52**, 3869–3879.
45 W. C. Stwalley, *Chem. Phys. Lett.*, 1970, **6**, 241–244.
46 K. T. Lu and U. Fano, *Phys. Rev. A: At., Mol., Opt. Phys.*, 1970, **2**, 81–86.
47 H. Jelassi, B. Viaris de Lesegno and L. Pruvost, *Phys. Rev. A: At., Mol., Opt. Phys.*, 2006, **74**, 012510.
48 H. Jelassi, B. Viaris de Lesegno, L. Pruvost, M. Pichler and W. C. Stwalley, *Phys. Rev. A: At., Mol., Opt. Phys.*, 2008, **78**, 022503.
49 D. Comparat, *J. Chem. Phys.*, 2004, **120**, 1318–1329.
50 H. Jelassi, B. Viaris de Lesegno and L. Pruvost, *Phys. Rev. A: At., Mol., Opt. Phys.*, 2008, **77**, 062515.
51 N. Bouloufa, A. Crubellier and O. Dulieu, *Phys. Rev. A: At., Mol., Opt. Phys.*, 2007, **75**, 052501.
52 Y. N. Demkov and V. N. Ostrovsky, *J. Phys. B: At., Mol., Opt. Phys.*, 1995, **28**, 403.
53 R. Leroy, *Can. J. Phys.*, 1972, **50**, 953–959.
54 M. Aymar and O. Dulieu, *J. Chem. Phys.*, 2005, **122**, 204302.
55 N. Spies, *PhD thesis*, Universität Kaiserslautern, 1989.
56 M. Vatasescu, O. Dulieu, C. Amiot, D. Comparat, C. Drag, V. Kokoouline, F. Masnou-Seeuws and P. Pillet, *Phys. Rev. A: At., Mol., Opt. Phys.*, 2000, **61**, 044701.
57 V. Kokoouline, O. Dulieu, R. Kosloff and F. Masnou-Seeuws, *J. Chem. Phys.*, 1999, **110**, 9865.

